Accepted Manuscript

Implications of inherent inhomogeneities in thin carbon fiber-based gas diffusion layers: A comparative modeling study

Pablo A. García-Salaberri, Iryna V. Zenyuk, Gisuk Hwang, Marcos Vera, Adam Z. Weber, Jeff T. Gostick

PII: S0013-4686(18)32075-9

DOI: 10.1016/j.electacta.2018.09.089

Reference: EA 32621

To appear in: *Electrochimica Acta*

Received Date: 24 August 2018

Accepted Date: 13 September 2018

Please cite this article as: P.A. García-Salaberri, I.V. Zenyuk, G. Hwang, M. Vera, A.Z. Weber, J.T. Gostick, Implications of inherent inhomogeneities in thin carbon fiber-based gas diffusion layers: A comparative modeling study, *Electrochimica Acta* (2018), doi: https://doi.org/10.1016/j.electacta.2018.09.089.

O_2/H_2 concentration

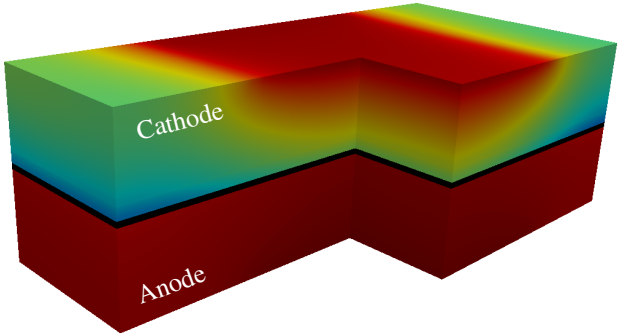

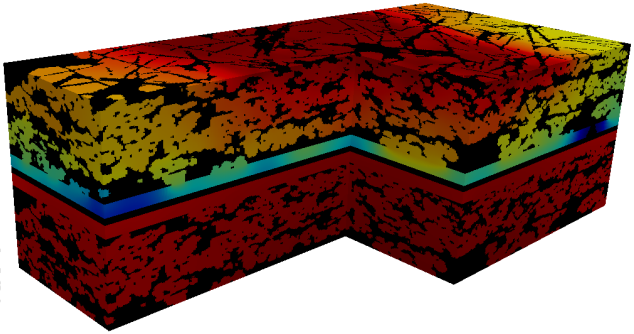

Temperature

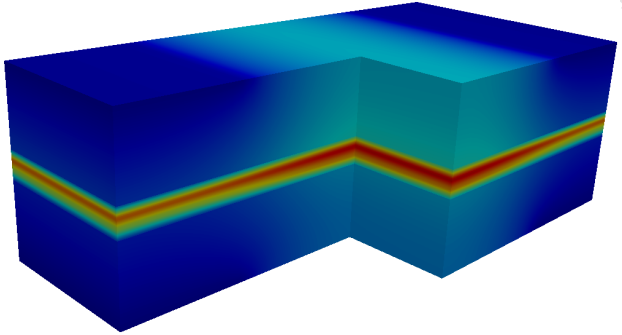

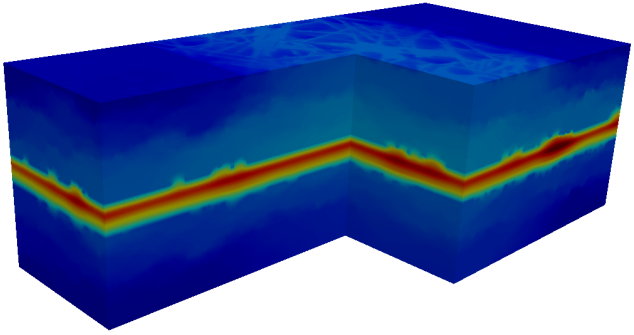

Implications of inherent inhomogeneities in thin carbon fiber-based gas diffusion layers: A comparative modeling study

Pablo A. García-Salaberri[1,*], Iryna V. Zenyuk[2], Gisuk Hwang[3], Marcos Vera[1], Adam Z. Weber[4] and Jeff T. Gostick[5]

[1] Departamento de Ingeniería Térmica y de Fluidos, Universidad Carlos III de Madrid, Leganés, 28911, Spain

[2] Department of Chemical Engineering and Material Science, National Fuel Cell Research Center, University of California, Irvine, CA 92697, USA

[3] Department of Mechanical Engineering, Wichita State University, Wichita, KS 67260, USA

[4] Energy Conversion Group, Lawrence Berkeley National Laboratory, Berkeley, CA 94720, USA

[5] Department of Chemical Engineering, University of Waterloo, Waterloo, ON N2L3G1, Canada

[*] Corresponding author: Tel: +34 91 624 9407 Fax: -

E-mail: pagsalab@ing.uc3m.es

URL: http://fluidosuc3m.es/people/pagsalab

Highlights

- Discrepancies of volume-averaged (VA) and pore-scale GDL models of a PEFC are examined
- VA models with suitable effective properties provide a good estimate for overall performance
- GDL inhomogeneities and interfacial phenomena influence predictions of VA models
- Impact of GDL microstructure on spatial distributions can affect durability modeling
- Interfacial design is a key control parameter for MEA manufacturing and assembly

Abstract

Thin porous media are present in multiple electrochemical energy devices, where they provide key transport and structural functions. The prototypical example is gas diffusion layers (GDLs) in polymer-electrolyte fuel cells (PEFCs). While modeling has often been used to explore PEFC operation, this is often accomplished using volume-averaged (VA) formulations, where the intrinsic inhomogeneities of the GDL are smoothed out and the lack of defining a representative elementary volume is an ever-present issue. In this work, the predictions of a single-phase VA PEFC model are compared to those of a pore-scale PEFC model using GDL tomograms as a part of the meshed domain to delineate important aspects that VA models cannot address. The results demonstrate that while VA models equipped with suitable effective properties can provide a good average estimate for overall performance, the lack of accounting for real structures limits their predictive power, especially for durability and degradation behavior where large deviations are found in the spatial distributions. Furthermore, interfacial effects between the GDL and the microporous layer are explored with the pore-scale model to understand the implications of the layered geometry. It is shown that the actual microstructure of the GDL/MPL transition region can significantly affect the fluxes across the sandwich, something that VA models cannot easily consider. Interfacial design is recognised as a crucial quality control parameter for large-scale MEA manufacturing and assembly.

Keywords: gas diffusion layer; polymer electrolyte fuel cell; modeling; inhomogeneities; pore scale

1. Introduction

Energy conversion and storage is viewed as a key element of a renewable energy economy. The leading technological options are electrochemical devices such as fuel cells, electrolyzers, and lithium-ion and redox flow batteries [1–5]. The polymer-electrolyte fuel cell (PEFC) is a particularly promising device as it can directly replace today's internal combustion engines in the transportation sector. PEFCs offer long range, short refueling times and high energy efficiency, and produce virtually zero emissions of air pollutants if hydrogen is produced from a renewable source (water and heat are the only products) [6]. Widespread commercialization of PEFCs is still forthcoming, however there are many applications where they are showing strong growth, such as materials handling vehicles in warehouses and fleets [7]. The core of a PEFC is the so-called membrane electrode assembly (MEA), which is composed of a central proton-exchange membrane (PEM), anode and cathode catalyst layers (CLs), and two backing gas diffusion layers (GDLs). A microporous layer (MPL) composed of a mixture of carbon black and PTFE is also coated onto the face of the GDL adjacent to the CL to alleviate flooding issues, improve hydration of the membrane, and reduce electrical and thermal interfacial or contact resistances [8–10]. The seven layers of the MEA are bonded together, and assembled between two bipolar plates (BPPs) for operation [11–13].

GDLs are a key multi-functional component as they mediate all transport processes occurring to and from the active catalyst sites. They are thin, highly porous materials consisting of non-woven carbon-fiber paper or woven carbon-fiber cloth [14,15]. A PTFE coating is also typically added to prevent wicking of liquid water throughout the pore space [16]. GDLs provide several critical functions: (i) a pathway for reactants access and products removal to/from the CLs, (ii) electrical and thermal conductivity, and (iii) adequate mechanical support to the MEA [17,18]. In fuel-cell applications, carbon

paper-based GDLs are the preferred option owing to their relatively good corrosion resistance, superior electrical conductivity, good gas transport properties, and higher mechanical stiffness compared to carbon cloth [19–21]. Besides, carbon-fiber papers typically show larger effective mass, charge and heat transport properties in the material plane owing to the preferential alignment of fibers and pores in that plane [22–24]. As a result, carbon-fiber papers are inherently inhomogeneous materials, consisting in a solid structure (fiber, binder and PTFE) and macro-pore network with average sizes in the order of 10-30 μm and 10-100 μm, respectively. Furthermore, uneven PTFE distribution creates non-uniform wettability, and land-channel geometry of BPPs induces additional inhomogeneity due to larger compression of the GDL under the lands [15,25,26].

Modeling of thin porous media, such as carbon fiber-based GDLs, has been an intense source of discussion for the past decade and continues to be today [27]. These materials have a much larger in-plane dimension than its thickness ($\delta_{\mathrm{gdl}} \sim 100 - 400\ \mu\mathrm{m}$), which typically spans no more than 10 pore sizes ($d_{\mathrm{p}} \sim 10 - 100\ \mu\mathrm{m}$). Hence, GDLs suffer from a lack of scale separation between their finite thickness and their inhomogeneous microstructure [27–29]. Moreover, the in-plane representative scale found in these materials ($\sim$ 1–2 mm) is comparable to the rib/channel width used in PEFCs [15,27,30,31]. This situation precludes a rigorous definition of a representative elementary volume (REV) within thin porous media. In layered assemblies, the definition of a REV is undermined even further due to the coupling between interfacial effects (layer-layer microstructure, real-world defects, material damage, etc.) and the lack of scale separation across the small thickness of the material [23,32–39,25]. These issues pose new modeling challenges that are not typically found in traditional porous media, such as soils and rocks, which warrant further analysis by the scientific community.

The most common approach used to model transport in GDLs, borrowed from the general porous-media literature [40,41], is macroscopic continuum modeling [42]. Macroscopic models are based on a volume-averaged (VA) formulation of mass,

momentum, species, charge and energy conservation equations, usually considering a macro-homogeneous description of the porous medium. The model is closed through appropriate constitutive relationships that define the effective properties of the GDLs, including diffusivity, permeability and electrical/thermal conductivity under single-phase conditions, and relative transport properties, capillary-pressure curve and phase-change kinetics under two-phase conditions [34]. The large body of work presented in the literature has shown that macroscopic models can be conveniently configured to describe overall performance and trends. However, the applicability of the continuum hypothesis to model thin, heterogeneous GDLs has been long questioned in the literature (see, e.g., [27–29] and references therein), and the source and amount of error incurred in the predictions of VA models is unclear.

Recently, great attention has been drawn to pore-scale (PS) modeling to overcome some of the shortcomings of VA GDL models, and improve our understanding of specific transport processes (see, e.g., [43–55] among others). Furthermore, PS models allow the characterization of effective properties that are extremely difficult to measure experimentally due to the small dimensions of GDLs [23,24,27,56–66]. Two main PS modeling approaches can be distinguished: pore-network modeling (PNM) and direct numerical simulation (DNS) [67,68]. PNMs idealize the pore space as a network of pore bodies interconnected by throats, whose size and connectivity are determined from the morphology of the porous medium [63]. Some authors have also presented dual networks that include both the solid phase and the standard fluid network [50,69]. Different transport processes can then be simulated on the networks, including capillary transport, convection, diffusion and heat conduction. On the other hand, DNS solves the transport equations (e.g., the heat or Navier-Stokes equations) on computational meshes generated on tomography images of the porous media, either using the lattice Boltzmann method (LBM) or conventional techniques, such as the finite-element (FEM) or finite-volume methods (FVM) [23,24,27,44,45]. This approach only requires the input of the bulk properties of the constituents of the material (e.g., the oxygen diffusion

coefficient in air for effective diffusivity), providing direct insight into the impact of the microstructure on transport processes. Consequently, the information that can be potentially extracted from DNS is richer, although its computational cost is significantly higher compared to PNM.

Currently, there is an increasing need to bridge the gap between VA and PS models in order to create more realistic but computationally efficient tools capable of guiding the design of MEAs, forecasting durability and diagnosing operation issues in the most self-predictive way as possible. This has motivated, for example, the development of hybrid VA-PNM/DNS models [43,49,50,70–72] and one-way multiscale models where effective properties extracted from PS simulations are plugged into VA models [44,45,73]. Inverse modeling techniques, such as global upscaling [74], have also been suggested as an efficient method to transfer local information from PS to VA models [27]. Nevertheless, the complex task of bridging the gap and constructing better simulation tools demands a deeper understanding of the discrepancies between VA and PS models. To the authors' knowledge, this modeling exercise has not been performed using a coupled multiphysics PEFC model that includes the full MEA. The only reference is the work of Rebai and Prat [28], who compared the water saturation profiles in GDLs predicted by a VA model and a PNM under water-injection conditions. They found that conventional VA models offer poor results of water distribution in GDLs due to the lack of REV in thin porous media and the dominance of capillary effects. Therefore, further effort is necessary.

In this work, the potential differences between VA and PS GDL descriptions are explored using a single-phase PEFC model. To this end, the anode and cathode GDL domains in a conventional VA model were replaced by tomograms of carbon paper-based GDLs, and transport was directly simulated on the microstructure. The effective transport properties (namely, diffusivity, permeability, and electrical and thermal conductivity) used in the VA model were computed on the same tomograms using the LBM, thereby enabling a one-to-one comparison. Moreover, two cases are analyzed by means of the

PS model, either including or not including intrusion of the MPL into the GDL to ascertain the impact of interfacial effects. The structure of the paper is as follows. The materials and X-ray tomography experiments are described in Section 2. In Section 3, the VA and PS models are presented, along with the operating conditions, geometrical parameters and key numerical considerations. In Section 4, the results are discussed, including a comparison of the polarization curves, 1D through-plane profiles and 2D in-plane distributions. In addition, an analysis of GDL/MPL intrusion and GDL surface region is presented. Finally, concluding remarks are given in Section 5.

2. Materials and X-ray tomography

X-ray tomography experiments were carried out at Advanced Light Source (ALS) synchrotron (beamline 8.3.2). Tomograms of uncompressed GDLs were acquired with a 3.5 mm field of view in the material plane and a resolution of 1.3 μm/voxel: untreated Toray® TGP-H-120 (full thickness, $\delta_{\mathrm{gdl}}^{\mathrm{ft}} = 367\ \mu\mathrm{m}$) and SIGRACET® SGL 25 AA ($\delta_{\mathrm{gdl}}^{\mathrm{ft}} = 195\ \mu\mathrm{m}$). Additional results for 10 wt% PTFE-treated TGP-H-120 and SGL 35 AA can be found in Supplementary Material. The above level of determination allowed us to capture the main characteristics of the GDL microstructure (pore and fiber diameter, $d_{\mathrm{p}} \sim 30 - 60\ \mu\mathrm{m}$ and $d_{\mathrm{f}} \sim 6 - 12\ \mu\mathrm{m}$). However, a precise differentiation of the constituents of the solid phase was not attempted due to their rather similar gray-scale values. Hence, homogeneous transport properties were assumed here for the entire solid phase [27]. In addition, the effect of nanoscale features, such as fiber roughness and contact points between fibers and binder, could not be resolved and should be explored in future work [51,75–79]. A thorough description of the experimental setup, the reconstruction of the image stacks, and the algorithm used to segment the gray-scale images into fluid and solid phases can be found elsewhere [23,24,27,45].

3. Numerical Modeling

3.1. Volume-averaged (VA) vs. pore-scale (PS) model

PEFC performance was modeled based on the 3D non-isothermal, steady-state volume-averaged model implemented by García-Salaberri et al. [80] in the FVM-based code ANSYS® Fluent. The mathematical formulation, including a detailed description of the conservation equations (i.e., mass, momentum, energy, species, electronic/ionic potentials and membrane water content), constitutive relationships and boundary conditions, is presented in Supplementary Material. As shown in Figure 1, an elementary differential cell comprising the seven layers of the MEA was used to explore the potential discrepancies between VA and PS GDL models. The first modeling approach considers a fully VA formulation equal to that used in the original model [80], while the second one includes GDL tomograms as a part of the meshed domain. A VA formulation was used for the remaining components (catalyst layers, microporous layers, membrane and bipolar plates), whose effective transport properties were kept equal to those assumed in [80]. Two cases were examined with the PS model: one that is geometrically equivalent to the VA model (hereafter denoted as PS), which neglects any intrusion of the MPL into the GDL, and another one that includes a uniform intrusion of 30 μm between the MPL and the GDL pore space (hereafter denoted as PS w/). The same effective transport properties were used for both the intruded and the core region of the MPL.

The effective anisotropic properties of the GDLs (diffusivity, permeability and electrical and thermal conductivity) were computed on the same tomograms used in the PS model by means of the LBM (see [27] for further details). The properties determined in the direction of the rib-channel pattern (*y*-direction) were used for both principal directions in the material plane. This methodology provided a direct link between the GDL tomograms and the effective properties of the VA model. As shown in Table 1, SGL 25 AA has a higher diffusivity and permeability ($f_{\mathrm{sgl}}/f_{\mathrm{tgp}}\sim1.4$, $K_{\mathrm{sgl}}/K_{\mathrm{tgp}}\sim4.7$) but a

significantly lower electrical and thermal conductivity ($\sigma_{\mathrm{sgl}}^{\mathrm{eff}}/\sigma_{\mathrm{tgp}}^{\mathrm{eff}}\sim0.2$, $k_{\mathrm{sgl}}^{\mathrm{eff}}/k_{\mathrm{tgp}}^{\mathrm{eff}}\sim0.3$) compared to TGP-H-120, as a result of its higher porosity and pore size ($\varepsilon_{\mathrm{sgl}}\approx0.8$, $d_{\mathrm{p,sgl}}\approx60\ \mu\mathrm{m}$ vs. $\varepsilon_{\mathrm{tgp}}\approx0.7$, $d_{\mathrm{p,tgp}}\approx30\ \mu\mathrm{m}$) [27]. On the other hand, the PS model was implemented using a direct mapping between the voxel image of the GDL and a hexahedral mesh created with the same spatial resolution in ANSYS® Fluent. Specifically, a binary mask containing the location of solid and fluid voxels was imported into the CFD code, and then the conforming solid and fluid regions were generated with the available unstructured meshing tools. Prior to this operation, a preprocessing step was performed in Matlab® to ensure that the GDL images contained only one solid and fluid region based on a 6-neighbor connectivity. That is, there were no closed pores or floating solids in the images. This step was critical to avoid numerical singularities, even though it involved minor changes in the images (less than 0.5% of the voxels interchanged their original solid/fluid label). Gas species transport was directly modeled on the fluid region by solving the Navier-Stokes and convection-diffusion equations with a wall boundary condition at the solid/fluid interface. Whereas, electron and heat conduction were modeled by solving either Laplace's or Poisson's equation in the entire GDL domain with a coupled boundary condition at the solid/fluid interface. The bulk electrical conductivities of the solid and fluid phases were fixed to $\sigma_{\mathrm{gdl}}^{\mathrm{solid}}=10^{5}\ \mathrm{S\ m^{-1}}$ and $\sigma_{\mathrm{gdl}}^{\mathrm{fluid}}=10^{-16}\ \mathrm{S\ m^{-1}}$, respectively, while the bulk thermal conductivity of the solid phase was set to $k_{\mathrm{gdl}}^{\mathrm{solid}}=70\ \mathrm{W\ m^{-1}\ K^{-1}}$. These values are comparable to those considered by other authors [57–59,76,78,81–86], and are equal to those used to scale the normalized effective properties computed with the LBM. The thermal conductivity of the gas phase was internally determined in ANSYS® Fluent according to the composition of the gas mixture (see Supplementary Material). Joule heating due to electron transport in the GDL was included in the solid phase.

3.2. Operational and geometrical parameters

The operational and geometrical parameters are summarized in Table 2. The air-feed

PEFC was simulated under high stoichiometric conditions ($\xi_a, \xi_c \gg 1$), using a temperature $T_{cell} = T_a^{in} = T_c^{in} = 80\ °C$, back-pressure $p_a^{out} = p_c^{out} = 1.5\ bar$, and relative humidity $RH_a^{in} = RH_c^{in} = 50\%$. These operating conditions avoided water condensation ($RH_{local} \geq 100\%$) except at high current densities ($I^{avg} \gtrsim 2\ A\ cm^{-1}$), thus providing a good scenario to perform a direct comparison between both modeling approaches. Typical geometrical dimensions were considered in the model: $w_{rib} = 0.936\ mm$, $w_{ch} = 1.014\ mm$, $H_{ch} = 1\ mm$, and $L_{ch} = 0.975\ mm$. The thicknesses of the VA components of the MEA were fixed to $\delta_{mpl} = 30\ \mu m$, $\delta_{cl} = 10\ \mu m$ and $\delta_{mem} = 20\ \mu m$, while the GDL thickness was varied according to the sample under consideration. As shown in Figure 2, the modeled GDL domain mostly included the core region of the material [27], so as to mimic the scenario of an assembled MEA that is substantially compressed. Nevertheless, a more detailed analysis of the impact of inhomogeneous compression due to the rib-channel pattern should be considered in future work [25,87]. The GDL thickness was equal to $\delta_{gdl} = 275\ \mu m$ for TGP-H-120 and $\delta_{gdl} = 130\ \mu m$ for SGL 25 AA, representing 75% and 67% of their full thickness, respectively. The same GDL tomograms were used at the anode and cathode sides, although interchanging the faces exposed to the MPL and the BPP. No important differences in the interfacial porosities and pore sizes of both interfaces were present in the samples examined.

3.3. Numerical considerations and solution

The GDL tomograms were down-sampled by a factor of 4 and 2 in the in- and through-plane directions, respectively, to reduce computational cost. The appropriate level of resolution was determined from LBM simulations that led to comparable effective anisotropic transport properties as those computed in images with a higher resolution. The computed values were also confirmed in calculations performed with ANSYS® Fluent using the same set-up of the LBM model [27]. In addition, the electronic potential was only solved at the cathode side to facilitate the interpretation of results and speed up

the simulations. The computational cost of the PS model to solve the 11 governing equations on meshes with around 20 million cells was around 1-2 weeks per cell voltage using 24-48 processors. Cases with a larger dependence on the interfacial microstructure of the solid phase ran longer due to the slower transmission of information throughout the numerical domain. On the contrary, the computational cost of the VA model was vastly lower, so that only several hours were necessary to compute a polarization curve using meshes with around 0.4 million cells and 8 processors. The set of partial differential equations was solved iteratively until convergence (residuals below 10^{-8}) using the pressure-based segregated solver with the SIMPLE algorithm, least square cell-based discretization for gradients, linear pressure interpolation and second-order upwind spatial discretization. The computational campaign, including test and validation simulations, was performed on the supercomputing cluster of the Fluid Mechanics Research Group at University Carlos III of Madrid and the cluster Orca of the SHARCNET supercomputing consortium in Canada [88,89].

4. Results and discussion

4.1. Polarization curve and through-plane profiles

Figure 3 shows the polarization curves computed for TGP-H-120 and SGL 25 AA with the VA model and the PS model without MPL intrusion. Additionally, the results of the PS model considering a uniform intrusion between the MPL and the GDL are included (see discussion in Section 4.3). The curves are consistent with those experimentally obtained using these materials [25,90–96], although since the study is focused on comparisons of models a rigorous fit to experimental data was not performed. The corresponding through-plane profiles across the MEA at $V_{\mathrm{cell}} = 0.5\ \mathrm{V}$ ($I^{\mathrm{avg}} \approx 1\ \mathrm{A\ cm^{-2}}$) are shown in Figure 4 for key variables of interest: cathode voltage drop, temperature, oxygen and hydrogen mass fractions, and RH.

The VA and PS models are geometrically equivalent, so they provide similar overall fluxes across the MEA and thus overall performance. This situation is particularly evident in the polarization curve and the through-plane profiles of TGP-H-120. However, the differences are larger for SGL 25 AA (ΔV_{cell}~10 mV @ $I^{\mathrm{avg}} = 1\ \mathrm{A\ cm^{-2}}$) due to its more porous and open microstructure, which leads to significant micrometer-scale electrical and thermal contact resistances at the GDL/MPL interface ($\varepsilon_{\mathrm{sgl,gdl/mpl}} \approx 0.8, d_{\mathrm{p,sgl}} \approx 60\ \mu\mathrm{m}$ vs. $\varepsilon_{\mathrm{tgp,gdl/mpl}} \approx 0.6, d_{\mathrm{p,tgp}} \approx 30\ \mu\mathrm{m}$). As a result, the electronic losses across the MPL-coated GDL are higher in the PS model, as are the ionic losses due to the slightly worse hydration of the membrane. Specifically, the GDL/MPL interfacial resistance arises from the combined effect of the finite interfacial area available for electron and heat transport (i.e., the interfacial solid fraction) and the finite conductivity of the MPL ($\sigma_{\mathrm{mpl}}^{\mathrm{eff}} = 300\ \mathrm{S\ m^{-1}}$, $k_{\mathrm{mpl}}^{\mathrm{eff}} = 0.1\ \mathrm{W\ m^{-1}\ K^{-1}}$). The micrometer-scale contact resistance at the GDL/BPP interface is significantly smaller because of the high conductivity of the BPP ($\sigma_{\mathrm{bpp}}^{\mathrm{eff}} = 2000\ \mathrm{S\ m^{-1}}$, $k_{\mathrm{bpp}}^{\mathrm{eff}} = 120\ \mathrm{W\ m^{-1}\ K^{-1}}$). As shown in Figure 4(b), the GDL/MPL electrical and thermal resistances lead to a sharp voltage and temperature drop between the MPL and the solid phase of the GDL (i.e., the electrically and thermally conductive phase), which cannot be captured by the VA model. Consequently, the VA model underestimates the temperature and voltage drop across the MPL-coated GDL.

The above results show that VA models can be a good approximation to predict overall performance provided that the model is equipped with appropriate effective transport properties, as was done here. However, the lack of a well-defined REV and finite-size interfacial resistances complicate the development of fully predictive models. In particular, the interfacial microstructure of the GDL can have significant effects on electrical, thermal and mass-transport fluxes across the sandwich but are typically neglected in VA models (see, e.g., [23,24,27,29,34,37,35,32,38,33,39,25,36] among others). Furthermore, the intrinsic inhomogeneous nature of GDLs, along with sheet-to-sheet and batch-to-batch manufacturing variations, warrant a cautious selection of the

effective properties used in VA models [27]. The picture is more confused under two-phase conditions, since liquid water transport is strongly impacted by microstructural characteristics, including among others: GDL pore and throat size and distribution, PTFE spatial dispersion, catalyst layer and MPL cracks and GDL surface roughness (see, e.g., [9,10,23,32,43,46,47,53–55,63,64,70,97–103]).

4.2. In-plane distributions

The inhomogeneities endemic to these materials can be visualized in the 2D distributions at $V_{\mathrm{cell}} = 0.5\ \mathrm{V}$ shown in Figures 5 and 6 for TGP-H-120 and SGL 25 AA, respectively. The variables include the current density, temperature and ionic resistance of the membrane, and oxygen mass fraction and RH in the CLs. The distributions in each figure have the same color scale to facilitate comparison, indicating the average value at the top of each subplot.

Significant differences are found in the spatial distributions of the VA and PS models since the VA domain is homogeneous, while the PS domain fully captures the geometry of the macro-porous GDL. The coupling between the rib/channel geometry, the microstructure of the GDL and local interfacial resistances leads to distributions with varying degree of complexity. A positive correlation was found between the local microstructure at the cathode GDL/MPL interface and the distributions in the cathode CL (oxygen mass fraction, RH and electronic potential) and the membrane temperature; see spatial correlations in Supplementary Material. The dependence of the membrane temperature on the cathode GDL/MPL microstructure is explained by the ten-fold lower thermal conductivity of air ($k_{\mathrm{air}} \sim 10^{-2}\ \mathrm{W\ m^{-1}\ K^{-1}}$) compared to hydrogen ($k_{\mathrm{H_2}} \sim 10^{-1}\ \mathrm{W\ m^{-1}\ K^{-1}}$), along with the similar porosities and pore sizes existent at the anode and cathode GDL/MPL interfaces. By comparing Figure 2 with Figures 5-6, it is seen that transport of oxygen and water vapor is favored in high-porosity regions, whereas heat and electron transport are promoted in low-porosity regions of the

cathode GDL/MPL interface. Transport of water vapor is, in turn, further enhanced in high-porosity regions of the cathode GDL/MPL interface due to the larger temperatures reached there. As a result, there is a preferential accumulation of water vapor (decrease of oxygen mass fraction) in dense solid regions of the cathode GDL/MPL interface. The effect that different anode and cathode microstructures have on in-plane distributions can be seen for PTFE-treated TGP-H-120 and SGL 35 AA in Supplementary Material.

The impact of GDL microstructure and its inherent inhomogeneity on the spatial distributions can have several practical implications, such as the formation of local hotspots and electrical resistances, oxygen-starved regions and water nucleation points that are smoothed out by VA models. For instance, the PS results presented here closely resemble the distributions measured by Wong et al. [104,105] by using fluorescence microscopy in a redox flow battery featuring carbon-paper electrodes. The extent of the variations between the spatial distributions of both models is shown in Figure 7. As can be seen, the average relative variations between both models are rather small, thus leading to comparable performance estimates. However, the local deviations amount more than 100% in the case of voltage drop, around 40-60% for oxygen mass fraction in the cathode CL, 10-30% for membrane resistance and RH in the CLs, and 10-20% for current density. These fluctuations can have important implications on degradation phenomena, where local conditions control degradation rates, or catalyst utilization estimates, where a region of catalyst can be starved of reactant. Durability modeling is an important building block for the community, which warrants the development of comprehensive multiscale VA models to improve our understanding of degradation mechanism from the nanoscale to the cell and stack level [34,106–108].

4.3. Interfacial effects: GDL/MPL intrusion and GDL surface region

The polarization curves, 1D profiles and 2D distributions of the PS model with GDL/MPL intrusion are shown in Figures 3, 4 and 5-6, respectively. The relative variations between

the PS models with and without MPL intrusion are presented in Figure 8 using a similar representation to that in Figure 7. The VA model was excluded from the analysis due to the hand-waviness of performing a one-to-one comparison. In particular, it would be necessary to add a 'second' MPL to the VA domain with different transport properties than the 'core' MPL, so as to account for the interfacial space occupied by solid carbon fibers.

The intrusion of the MPL into the GDL has two fundamental effects: (1) it decreases the reactant concentration and increases the water vapor concentration in the CLs, and (2) it reduces the micrometer-scale contact resistances at the GDL/MPL interface due to the better contact between these two layers. The reduction of the electrical contact resistance is strong (both at the anode and the cathode sides) due to the much larger electrical conductivity of the MPL compared to gas species ($\sigma_{\mathrm{mpl}}^{\mathrm{eff}} = 300\ \mathrm{S\ m^{-1}}$ vs. $\sigma_{\mathrm{gas}} = 10^{-16}\ \mathrm{S\ m^{-1}}$). In terms of heat transport, the impact of MPL intrusion is larger at the cathode since the thermal conductivity of the MPL is ten-fold higher than that of air ($k_{\mathrm{mpl}}^{\mathrm{eff}} = 10^{-1}\ \mathrm{W\ m^{-1}\ K^{-1}}$ vs. $k_{\mathrm{air}} \sim 10^{-2}\ \mathrm{W\ m^{-1}\ K^{-1}}$). However, the impact at the anode is rather small because the thermal conductivity of the MPL is similar to that of hydrogen ($k_{\mathrm{H_2}} \sim 10^{-1}\ \mathrm{W\ m^{-1}\ K^{-1}}$). As shown in Figure 3, these two effects lead to significant changes in the polarization curves. In the case of TGP-H-120, the limiting current density is dramatically reduced due to the additional mass transport resistance offered by the intruded portion of the MPL ($\Delta V_{\mathrm{cell}} \sim 100\ \mathrm{mV}$ @ $I^{\mathrm{avg}} = 1.8\ \mathrm{A\ cm^{-2}}$). In the case of SGL 25 AA, the decrease of the GDL/MPL electrical and thermal resistances, along with the better hydration of the membrane, make more similar the predictions of both models in terms of cell performance.

The effect of the GDL surface region in the case of SGL 25 AA is examined next. As depicted in Figure 9, starting from the base case mostly including the core region of the material (black patch), several GDL domains were analyzed by gradually adding an extra portion of the thickness (purple to yellow patches). Five domains were simulated in

total, including the one used in the previous sections. The thicknesses examined are equal to 130, 143, 156, 169 and 182 μm, corresponding to $\delta_{\mathrm{gdl}}/\delta_{\mathrm{gdl}}^{\mathrm{ft}} = 67$, 73, 80, 87 and 93% of the full thickness, respectively. Figure 9 also shows the Euclidean transform of the GDL pore space at the anode and cathode MPL interfaces, where it is seen that the interfacial porosity and pore size increase from around 0.85 to 0.95 and 80 μm to 200 μm as the GDL window length is enlarged.

The variation of the average current density and cathode voltage drop at $V_{\mathrm{cell}} = 0.5$ V as a function of the GDL window length is shown in Figure 10(a). As can be seen, the highly-porous surface region leads to a strong decrease of the current density when MPL intrusion is neglected, decreasing from 1 A cm^{-2} ($\delta_{\mathrm{gdl}}/\delta_{\mathrm{gdl}}^{\mathrm{ft}} = 0.67$) to 0.65 A cm^{-2} ($\delta_{\mathrm{gdl}}/\delta_{\mathrm{gdl}}^{\mathrm{ft}} = 0.93$). The reduction of the performance arises from the voltage drop created by the micro-scale electrical contact resistance at the GDL/MPL interface. As shown in Figure 10(b, left), the cathode voltage drop increases non-linearly from 10 mV to more than 70 mV as a larger portion of the surface region is included. The electrical contact resistance, as discussed earlier, is manifested as a sharp voltage drop between the MPL and the solid phase of the GDL, while the gas phase of the GDL (80% of the material) remains passively close to the mean; see the example in Figure 10(b, right). By way of contrast, the current density predicted by the PS model with MPL intrusion prevails relatively constant around 1 A cm^{-2}, since the impact of contact resistances is significantly reduced. The slight decline of the performance in this case is caused by the decrease of the effective electrical and thermal conductivity of the GDL by the effect of the surface region (see Table 1), which increases the electronic losses in the GDL and the ionic losses in the membrane (worse hydration). These results show the sensitivity of thin porous media to local conditions [23], highlighting the importance of interfaces as a key control and quality parameter for large-scale MEA manufacturing.

5. Conclusions

In this work, the effect of the inherent inhomogeneities of carbon paper-based gas diffusion layers (GDLs) used in polymer-electrolyte fuel cells (PEFCs) were examined. This is important information for the development of more comprehensive multiscale models, as well as to improve our understanding of transport processes in PEFCs as the model fidelity is increased. To thin end, single-phase PEFC performance was simulated on a 2x1 mm^2 differential cell considering both a volume-averaged (VA) and a pore-scale (PS) description for the GDL. The PS model was equipped with micro-tomographies of the GDL as a part of the meshed domain, employing a VA formulation for the remaining layers of the membrane electrode assembly (MEA). In addition, the effective properties of the GDL in the VA model (i.e., diffusivity, permeability, and electrical and thermal conductivity) were extracted from lattice-Boltzmann simulations performed on the same tomographies. This enabled a direct comparison between both modeling approaches. Additionally, the partial intrusion between the GDL and the microporous layer (MPL), as well as the GDL surface region, were examined by means of the PS model to ascertain the effect of interfacial phenomena.

It was found that VA models of GDLs accounting for suitable effective properties provide good estimates for aggregated quantities such as overall cell performance, even though their predictive power is limited by (1) the lack of a well-defined representative elementary volume in thin GDLs and (2) finite-size interfacial resistances in layered assemblies. Besides, the selection of effective transport properties can be problematic due to sheet-to-sheet and batch-to-batch heterogeneities existent in GDLs. This issue was overcome here by using a direct link between the modeled GDL microstructure and the effective properties considered in the VA model, but can, in general, lead to non-negligible differences. In this study, the larger discrepancies between the VA and PS models were observed in the spatial distributions, since the VA model smoothed out oxygen-starved regions, water nucleation points, hotspots and local electrical resistances compared to the PS model. These inherent inhomogeneities are expected to affect

degradation phenomena and deserve further investigation by the community in multiscale degradation analyses. In addition, a large impact of interfacial effects between the GDL and the MPL on cell performance was found due to the sensitivity of through-plane fluxes across the MEA to local conditions between layers. The appropriate design of interfaces is a key engineering aspect to be considered for quality control in MEA manufacturing and assembly.

In summary, this work highlighted that using macro-homogeneous VA models to describe GDLs should be taken with care, even though they are the de-facto choice to simulate large domains due to their rather low computational cost. In this regard, PS modeling must be considered as a complementary technique to analyze the complex multiscale behavior of PEFCs and guide the construction of more advanced multiscale VA models, especially where material heterogeneities play critical roles. Generally speaking, two aspects has been identified in this work to upgrade the predictive capabilities of VA models: (1) to incorporate the effect of GDL bulk inhomogeneities, and (2) to improve the modeling of interfacial phenomena. Additional exercises that should be considered in future work include the analysis of tomograms of catalyst layers and commercial MPL-coated GDLs, nanoscale contact details, inhomogeneous assembly compression and two-phase transport.

Acknowledgements

The authors thank the support team of Calcul Québec, SHARCNET and Compute Canada and Dr. Sánchez-Monreal at Universidad Carlos III of Madrid (UC3M) for their help during the simulation campaign, as well as Dr. Dula Parkinson and Dr. Alastair MacDowell at the Advanced Light Source (ALS) for help in obtaining the tomographic images. This work was funded under the Fuel Cell Performance and Durability Consortium (FC-PAD), by the Fuel Cell Technologies Office (FCTO), Office of Energy Efficiency and Renewable Energy (EERE), of the U.S. Department of Energy under contract number DE-AC02-05CH11231,

the Project ENE2015-68703-C2-1-R (MINECO/FEDER, UE), and the the research grant 'Ayudas a la Investigación en Energía y Medio Ambiente' awarded to the first author by the Spanish Iberdrola Foundation. Dr. Iryna V. Zenyuk would like to acknowledge support from the National Science Foundation under CBET Award 1605159. X-ray tomography experiments were performed on beamline 8.3.2 at the ALS, which is a national user facility funded by the Department of Energy, Office of Basic Energy Sciences under contract DE-AC02-05CH11231. Simulations were made on the supercomputing clusters of Calcul Québec, SHARCNET, Compute Canada and the Fluid Mechanics Research Group at UC3M.

Nomenclature

Symbols

d	diameter [m]
f	normalized effective gas-phase diffusivity [-]
H	height [m]
I	current density [A m^{-2}]
K	permeability [m^2]
k	thermal conductivity [W m^{-1} K^{-1}]
L	longitudinal length in y-direction [m]
p	pressure [Pa]
Q	volumetric flow rate [m^3 s^{-1}]
R	ionic resistance [Ω m^2]
RH	relative humidity [-]
T	temperature [K]
V_{cell}	cell voltage [V]
w	width [m]
x	in-plane coordinate [m]
Y_{i}	mass fraction of species i [-]

y secondary in-plane coordinate [m]

z through-plane coordinate [m]

Greek letters

Δ increment

δ thickness [m]

ε porosity [-]

ε_{i} area-averaged porosity in i-direction [-]

ξ stoichiometric flow ratio [-]

σ electrical conductivity [S m^{-1}]

ϕ_{e^-} electronic potential [V]

Subscripts

a anode

bpp bipolar plate

c cathode

ch channel

cl catalyst layer

cl-bpp between cl and bpp

f fiber

gdl gas diffusion layer

ip in-plane direction

mem membrane

mpl microporous layer

p pore

rib bipolar plate rib

tp through-plane direction

Superscripts

avg average

eff effective property

fluid GDL fluid region

ft full thickness

solid GDL solid region

Abbreviations & acronyms

BPP bipolar plate

CL catalyst layer

CR core region

DNS direct numerical simulation

FT full thickness

GDL gas diffusion layer

IP in-plane

LBM lattice Boltzmann method

MEA membrane electrode assembly

MPL microporous layer

PEFC polymer-electrolyte fuel cell

PEM polymer-electrolyte membrane

PNM pore-network modeling

PS pore scale

PTFE polytetrafluoroethylene

REV representative elementary volume

SR surface region

TP through-plane

VA volume averaged

X-CT X-ray computed tomography

References

[1] F. Díaz-González, A. Sumper, O. Gomis-Bellmunt, R. Villafáfila-Robles, Renew. Sustain. Energy Rev. 16 (2012) 2154–2171.

[2] L. Barreto, A. Makihira, K. Riahi, Int. J. Hydrogen Energy 28 (2003) 267–284.

[3] R. Dell, D.A. Rand, J. Power Sources 100 (2001) 2–17.

[4] M.H. Nehrir, C. Wang, K. Strunz, H. Aki, R. Ramakumar, J. Bing, Z. Miao, Z. Salameh, IEEE Trans. Sustain. Energy 2 (2011) 392–403.

[5] A.Z. Weber, M.M. Mench, J.P. Meyers, P.N. Ross, J.T. Gostick, Q. Liu, J. Appl. Electrochem. 41 (2011) 1137–1164.

[6] M.W. Ellis, M.R. Von Spakovsky, D.J. Nelson, Proc. IEEE 89 (2001) 1808–1818.

[7] O.Z. Sharaf, M.F. Orhan, Renew. Sustain. Energy Rev. 32 (2014) 810–853.

[8] S.G. Kandlikar, M.L. Garofalo, Z. Lu, Fuel Cells 11 (2011) 814–823.

[9] A.Z. Weber, J. Newman, J. Electrochem. Soc. 152 (2005) A677–A688.

[10] J.T. Gostick, M.A. Ioannidis, M.W. Fowler, M.D. Pritzker, Electrochem. Commun. 11 (2009) 576–579.

[11] V. Mehta, J.S. Cooper, J. Power Sources 114 (2003) 32–53.

[12] S. Litster, G. McLean, J. Power Sources 130 (2004) 61–76.

[13] X. Li, I. Sabir, Int. J. Hydrogen Energy 30 (2005) 359–371.

[14] M. Mathias, J. Roth, J. Fleming, W. Lehnert (Chapter 46), in: W. Vielstich, H.A. Gasteiger, A. Lamm (Eds.), Handbook of Fuel Cells-fundamentals, Technology and Applications, Fuel Cell Technology and Applications, vol. 3, John Wiley & Sons, Ltd, 2003.

[15] I.V. Zenyuk, D.Y. Parkinson, L.G. Connolly, A.Z. Weber, J. Power Sources 328 (2016) 364–376.

[16] C. Lim, C.Y. Wang, Electrochim. Acta 49 (2004) 4149–4156.

[17] L. Cindrella, A. M. Kannan, J.F. Lin, K. Saminathan, Y. Ho, C.W. Lin, J. Wertz, J. Power Sources 194 (2009) 146–160.

[18] S. Park, J.W. Lee, B.N. Popov, Int. J. Hydrogen Energy 37 (2012) 5850–5865.

[19] V. Radhakrishnan, P. Haridoss, Mater. Des. 32 (2011) 861–868.

[20] R.P. O'Hayre, S.W. Cha, W.G. Colella, F.B. Prinz, Fuel Cell Fundamentals, second ed., Wiley, New York, 2009.

[21] Y. Wang, C.Y. Wang, K.S. Chen, Electrochim. Acta 52 (2007).

[22] R. Flückiger, S.A. Freunberger, D. Kramer, A. Wokaun, G.G. Scherer, F.N. Büchi, Electrochim. Acta 54 (2008) 551–559.

[23] P.A. García-Salaberri, G. Hwang, M. Vera, A.Z. Weber, J.T. Gostick, Int. J. Heat Mass Transf. 86 (2015) 319–333.

[24] P.A. García-Salaberri, J.T. Gostick, G. Hwang, A.Z. Weber, M. Vera, J. Power Sources 296 (2015) 440–453.

[25] R.W. Atkinson, Y. Garsany, B.D. Gould, K.E. Swider-Lyons, I.V. Zenyuk, ACS Appl. Energy Mater. 1 (2017) 191–201.

[26] I. V. Zenyuk, D.Y. Parkinson, G. Hwang, A.Z. Weber, Electrochem. Commun. 53

(2015) 24–28.

[27] P.A. García-Salaberri, I.V. Zenyuk, A.D. Shum, G. Hwang, M. Vera, A.Z. Weber, J.T. Gostick, Analysis of representative elementary volume and through-plane regional characteristics of carbon-fiber papers: diffusivity, permeability and electrical/thermal conductivity, Int. J. Heat Mass Transf. 127 (2018) 687–703.

[28] M. Rebai, M. Prat, J. Power Sources 192 (2009) 534–543.

[29] M. Prat, T. Agaësse, Thin Porous Media, Handb. Porous Media 3rd ed., 89–112, Taylor & Francis, London, 2015.

[30] A.D. Santamaria, P.K. Das, J.C. MacDonald, A.Z. Weber, J. Electrochem. Soc. 161 (2014) F1184–F1193.

[31] J. Roth, J. Eller, F. Marone, F.N. Büchi, J. Phys. Chem. C 117 (2013) 25991–25999.

[32] I.V. Zenyuk, R. Taspinar, A.R. Kalidindi, E.C. Kumbur, S. Litster, J. Electrochem. Soc. 161 (2014) F3091–F3103.

[33] I.V. Zenyuk, E.C. Kumbur, S. Litster, J. Power Sources 241 (2013) 379–387.

[34] A.Z. Weber, R.L. Borup, R.M. Darling, P.K. Das, T.J. Dursch, W. Gu, D. Harvey, A. Kusoglu, S. Litster, M.M. Mench, R. Mukundan, J.P. Owejan, J.G. Pharoah, M. Secanell, I.V. Zenyuk, J. Electrochem. Soc. 161 (2014) F1254–F1299.

[35] D. Qiu, L. Peng, P. Yi, X. Lai, H. Janßen, W. Lehnert, ECS Trans. 80 (2017) 73–85.

[36] A. Wong, A. Bazylak, ECS Trans. 80 (2017) 175–186.

[37] C. Simon, F. Hasché, H.A. Gasteiger, J. Electrochem. Soc 164 (2017) F591–F599.

[38] D. Qiu, L. Peng, P. Yi, X. Lai, Int. J. Mech. Sci. 124–125 (2017) 37–47.

[39] Q. Meyer, N. Mansor, F. Iacoviello, P.L. Cullen, R. Jervis, D. Finegan, C. Tan, J. Bailey, P.R. Shearing, D.J.L. Brett, Electrochim. Acta 242 (2017) 125–136.

[40] S. Whitaker, The Method of Volume Averaging, Kluwer Academic Publishers, Boston, 1999.

[41] J. Bear, J.M. Buchlin, Modeling and Application of Transport Phenomena in Porous Media, Kluwer Academic Publishers, Boston, 1991.

[42] C.Y. Wang, Chem. Rev. 104 (2004) 4727–65.

[43] N. Belgacem, M. Prat, J. Pauchet, Int. J. Hydrogen Energy 42 (2017) 8150–8165.

[44] M. Sabharwal, L.M. Pant, A. Putz, D. Susac, J. Jankovic, M. Secanell, Fuel Cells 16 (2016) 734–753.

[45] P.A. García-Salaberri, J.T. Gostick, I.V. Zenyuk, G. Hwang, M. Vera, A.Z. Weber, ECS Trans. 80 (2017) 133–143.

[46] M.A. Safi, N.I. Prasianakis, J. Mantzaras, A. Lamibrac, F.N. Büchi, Int. J. Heat Mass Transf. 115 (2017) 238–249.

[47] P. Satjaritanun, J.W. Weidner, S. Hirano, Z. Lu, Y. Khunatorn, S. Ogawa, S.E. Litster,

A.D. Shum, I.V. Zenyuk, S. Shimpalee, J. Electrochem. Soc. 164 (2017) E3359–E3371.

[48] T.G. Tranter, J.T. Gostick, A.D. Burns, W.F. Gale, Transp. Porous Media (2017) 1–24.

[49] E.F. Medici, I.V. Zenyuk, D.Y. Parkinson, A.Z. Weber, J.S. Allen, Fuel Cells 16 (2016) 725–733.

[50] M. Aghighi, J. Gostick, J. Appl. Electrochem. 47 (2017) 1323–1338.

[51] H. Liu, J. Hinebaugh, S. Chevalier, R. Banerjee, C.H. Lee, A. Bazylak, Transp. Porous Media (2017) 1–22.

[52] C. Qin, J. Electrochem. Soc. 162 (2015) F1036–F1046.

[53] K. Seidenberger, F. Wilhelm, J. Haußmann, H. Markötter, I. Manke, J. Scholta, J. Power Sources 239 (2013) 628–641.

[54] P.K. Sinha, C.Y. Wang, Electrochim. Acta 52 (2007) 7936–7945.

[55] J. Hinebaugh, A. Bazylak, J. Electrochem. Soc. 157 (2010) B1382– B1390.

[56] S. Hasanpour, M. Hoorfar, A.B. Phillion, J. Power Sources 353 (2017) 221–229.

[57] A. Pfrang, D. Veyret, F. Sieker, G. Tsotridis, Int. J. Hydrogen Energy 35 (2010) 3751–3757.

[58] N. Zamel, X. Li, J. Shen, J. Becker, A. Wiegmann, Chem. Eng. Sci. 65 (2010) 3994–4006.

[59] M. Göbel, M. Godehardt, K. Schladitz, J. Power Sources 355 (2017) 8–17.

[60] T. Rosén, J. Eller, J. Kang, N.I. Prasianakis, J. Mantzaras, F.N. Buchi, J. Electrochem. Soc. 159 (2012) F536–F544.

[61] A. Nabovati, E.W. Llewellin, A.C.M. Sousa, Compos. Part A Appl. Sci. Manuf. 40 (2009) 860–869.

[62] Y. Gao, Z. Hou, X. Wu, P. Xu, Int. J. Heat Mass Transf. 118 (2018) 1325–1339.

[63] J.T. Gostick, M.A. Ioannidis, M.W. Fowler, M.D. Pritzker, J. Power Sources 173 (2007) 277–290.

[64] J.T. Gostick, J. Electrochem. Soc. 160 (2013) F731–F743.

[65] L. Holzer, O. Pecho, J. Schumacher, P. Marmet, F.N. Büchi, A. Lamibrac, B. Münch, Electrochim. Acta 241 (2017) 414–432.

[66] L. Holzer, O. Pecho, J. Schumacher, P. Marmet, O. Stenzel, F.N. Büchi, A. Lamibrac, B. Münch, Electrochim. Acta 227 (2017) 419–434.

[67] A. Arvay, E. Yli-Rantala, C.H. Liu, X.H. Peng, P. Koski, L. Cindrella, P. Kauranen, P.M. Wilde, A.M. Kannan, J. Power Sources 213 (2012) 317–337.

[68] P.P. Mukherjee, Q. Kang, C.Y. Wang, Energy Environ. Sci. 4 (2011) 346–369.

[69] V. Konduru, J.S. Allen, ECS Trans. 80 (2017) 65–71.

[70] M. Aghighi, M.A. Hoeh, W. Lehnert, G. Merle, J. Gostick, J. Electrochem. Soc. 163 (2016) F384–F392.

[71] L. Chen, H. Luan, Y. Feng, C. Song, Y.L. He, W.Q. Tao, Int. J. Heat Mass Transf. 55 (2012) 3834–3848.

[72] I.V. Zenyuk, E. Medici, J. Allen, A.Z. Weber, Int. J. Hydrogen Energy 40 (2015) 16831–16845.

[73] S.K. Babu, H.T. Chung, P. Zelenay, S. Litster, J. Electrochem. Soc. 164 (2017) F1037–F1049.

[74] L. Holden, B.F. Nielsen, Transp. Porous Media. 40 (2000) 115–143.

[75] H. Sadeghifar, N. Djilali, M. Bahrami, J. Power Sources 248 (2014) 632–641.

[76] E. Sadeghi, N. Djilali, M. Bahrami, J. Power Sources 196 (2011) 246–254.

[77] H. Sadeghifar, M. Bahrami, N. Djilali, J. Power Sources 233 (2013) 369–379.

[78] E. Sadeghi, M. Bahrami, N. Djilali, J. Power Sources 179 (2008) 200–208.

[79] J. Eller, A. Lamibrac, F. Marone, F.N. Büchi, Influence of Binder Porosity on Gdl Gas Phase Transport, ECS Meeting Abstracts MA2016-02 2747, 2016.

[80] P.A. García-Salaberri, D.G. Sánchez, P. Boillat, M. Vera, K.A. Friedrich, J. Power Sources 359 (2017) 634–655.

[81] A. Pfrang, D. Veyret, G. Tsotridis, Computation of Thermal Conductivity of Gas Diffusion Layers of PEM Fuel Cells, in: A. Ahsan (Ed.), Convection and Conduction Heat Transfer, InTech, 2011.

[82] J. Yablecki, A. Bazylak, J. Power Sources 217 (2012) 470–478.

[83] J. Yablecki, A. Nabovati, A. Bazylak, J. Electrochem. Soc. 159 (2012) B647–B653.

[84] J. Ramousse, S. Didierjean, O. Lottin, D. Maillet, Int. J. Therm. Sci. 47 (2008) 1–6.

[85] H. Sadeghifar, N. Djilali, M. Bahrami, Int. J. Hydrogen Energy 41 (2016) 6833–6841.

[86] J. Becker, R. Flückiger, M. Reum, F.N. Büchi, F. Marone, M. Stampanoni, J. Electrochem. Soc. 156 (2009) B1175–B1181.

[87] P.A. García-Salaberri, M. Vera, R. Zaera, Int. J. Hydrogen Energy 36 (2011) 11856–11870.

[88] http://fluidosuc3m.es/

[89] https://www.sharcnet.ca/

[90] J. Zhou, S. Shukla, A. Putz, M. Secanell, Electrochim. Acta. 268 (2018) 366-382.

[91] I. V. Zenyuk, P.K. Das, A.Z. Weber, J. Electrochem. Soc. 163 (2016) F691–F703.

[92] P.M. Wilde, M. Mändle, M. Murata, N. Berg, (2004) 180–184.

[93] D.G. Sanchez, D.G. Diaz, R. Hiesgen, I. Wehl, K.A. Friedrich, J. Electroanal. Chem. 649 (2010) 219–231.

[94] J. Kleemann, F. Finsterwalder, W. Tillmetz, J. Power Sources 190 (2009) 92–102.

[95] T. Bednarek, G. Tsotridis, J. Power Sources 343 (2017) 550–563.
[96] E. Yli-Rantala, P. Koski, M. Kotisaari, S. Auvinen, M. Karhu, J. Nikkola, P. Kauranen, A. Puolakka, P. Heikkilä, Advanced Material Solutions for PEM Fuel Cells, final report, Tampere, 2012.
[97] J. Eller, J. Roth, F. Marone, M. Stampanoni, F.N. Büchi, J. Electrochem. Soc. 164 (2017) F115–F126.
[98] J. Eller, T. Rosén, F. Marone, M. Stampanoni, A. Wokaun, F.N. Büchi, J. Electrochem. Soc. 158 (2011) B963–B970.
[99] A. Lamibrac, J. Roth, M. Toulec, F. Marone, M. Stampanoni, F.N. Büchi, J. Electrochem. Soc. 163 (2016) F202–F209.
[100] A. Jarauta, M. Secanell, J. Pons-Prats, P. Ryzhakov, S.R. Idelsohn, E. Oñate, Int. J. Hydrogen Energy 40 (2015) 5375–5383.
[101] A. Jarauta, P. Ryzhakov, M. Secanell, P.R. Waghmare, J. Pons-Prats, J. Power Sources 323 (2016) 201–212.
[102] P.B. Ryzhakov, A. Jarauta, M. Secanell, J. Pons-Prats, Comput. Part. Mech. 4 (2017) 285–295.
[103] J. Yu, D. Froning, U. Reimer, W. Lehnert, Int. J. Hydrogen Energy 43 (2018) 6318–6330.
[104] A.A. Wong, M.J. Aziz, S. Rubinstein, ECS Trans. 77 (2017) 153–161.
[105] A.A. Wong, S. Rubinstein, M.J. Aziz, ECS Meeting Abstracts MA2017-02 19, 2017.
[106] M. Hasan, A. Goshtasbi, T. Ersal, J. Chen, M.H. Santare, J. Electrochem. Soc. 165 (2018) F3359–F3372.
[107] R. Singh, P.C. Sui, K.H. Wong, E. Kjeang, J. Electrochem. Soc. 165 (2018) F3328–F3336.
[108] T. Jahnke, G. Futter, A. Latz, T. Malkow, G. Papakonstantinou, G. Tsotridis, P. Schott, M. Gérard, M. Quinaud, M. Quiroga, A.A. Franco, K. Malek, F. Calle-Vallejo, R. Ferreira De Morais, T. Kerber, P. Sautet, D. Loffreda, S. Strahl, M. Serra, P. Polverino, C. Pianese, M. Mayur, W.G. Bessler, C. Kompis, J. Power Sources 304 (2016) 207–233.

Table 1: Effective anisotropic transport properties of the GDLs, as determined from LBM simulations.

GDL	Porosity, ε	TP/IP normalized diffusivity, $f_{\mathrm{tp}} \,/\, f_{\mathrm{ip}}\ [-]$	TP/IP permeability, $K_{\mathrm{tp}} \,/\, K_{\mathrm{ip}}\ [\mathrm{m}^2]$ $(\times 10^{11})$	TP/IP electrical conductivity, $\sigma_{\mathrm{tp}}^{\mathrm{eff}}/\sigma_{\mathrm{ip}}^{\mathrm{eff}}\ [\mathrm{S\ cm^{-1}}]$	TP/IP thermal conductivity, $k_{\mathrm{tp}}^{\mathrm{eff}} \,/\, k_{\mathrm{ip}}^{\mathrm{eff}}$ $[\mathrm{W\ m^{-1}\ K^{-1}}]$
TGP-H-120 (0 wt%)	0.66	0.2/0.35	0.3/0.55	53/170	3.8/11.6
SGL 25 AA ($\delta_{\mathrm{gdl}} = 130, 143, 156, 169, 182\ \mu\mathrm{m}$)	0.75, 0.76, 0.77, 0.79, 0.8	0.3/0.55, 0.31/0.58, 0.32/0.61, 0.33/0.63, 0.35/0.65	1/1.5, 1.05/1.6, 1.1/1.7, 1.15/1.9, 1.2/2.2	16/125, 13/118, 9/110, 5/104, 2.4/97	1.2/8.8, 0.95/8.4, 0.7/7.8, 0.5/7.4, 0.25/7

Table 2: Operational and geometrical parameters (see boundary conditions in Supplementary Material).

Parameter	Symbol	Value
Operational parameters		
Hydrogen feed flow rate / sccm	$Q_{\mathrm{H_2}}$	800 ($\xi_{\mathrm{a}} = 5.8 \times 10^3$ @ 1 A cm^{-2})
Air feed flow rate / sccm	Q_{air}	1100 ($\xi_{\mathrm{c}} = 3.3 \times 10^3$ @ 1 A cm^{-2})
Cell temperature / $^{\mathrm{o}}$C	T_{cell}	80
Anode and cathode inlet temperature / $^{\mathrm{o}}$C	$T_{\mathrm{a}}^{\mathrm{in}}, T_{\mathrm{c}}^{\mathrm{in}}$	80
Anode and cathode back-pressure / bar	$p_{\mathrm{a}}^{\mathrm{out}}, p_{\mathrm{c}}^{\mathrm{out}}$	1.5
Anode and cathode inlet RH / -	$\mathrm{RH}_{\mathrm{a}}^{\mathrm{in}}, \mathrm{RH}_{\mathrm{c}}^{\mathrm{in}}$	0.5 (50%)
Geometrical parameters		
Rib width / mm	w_{rib}	0.936
Channel width / mm	w_{ch}	1.014
Channel height / mm	H_{ch}	1
Channel length / mm	L_{ch}	0.975
GDL thickness (TGP-H-120, SGL 25 AA) / μm	δ_{gdl}	275, 130[a]
MPL thickness / μm	δ_{mpl}	30[b]
CL thickness / μm	δ_{cl}	10
PEM thickness / μm	δ_{mem}	20

a Four extra GDL thicknesses are considered in Section 4.3 to examine the effect of the surface region of SGL 25 AA: $\delta_{\mathrm{gdl}} = 143, 156, 169$ and 182 μm. The full thicknesses of the main samples of TGP-H-120 and SGL 25 AA are $\delta_{\mathrm{gdl}}^{\mathrm{ft}} = 367$ μm and $\delta_{\mathrm{gdl}}^{\mathrm{ft}} = 195$ μm, respectively.

b The effect of MPL intrusion is examined in Section 4.3 considering a uniform intrusion of 30 μm between the MPL and the GDL pore space (in addition to the core region of 30 μm).

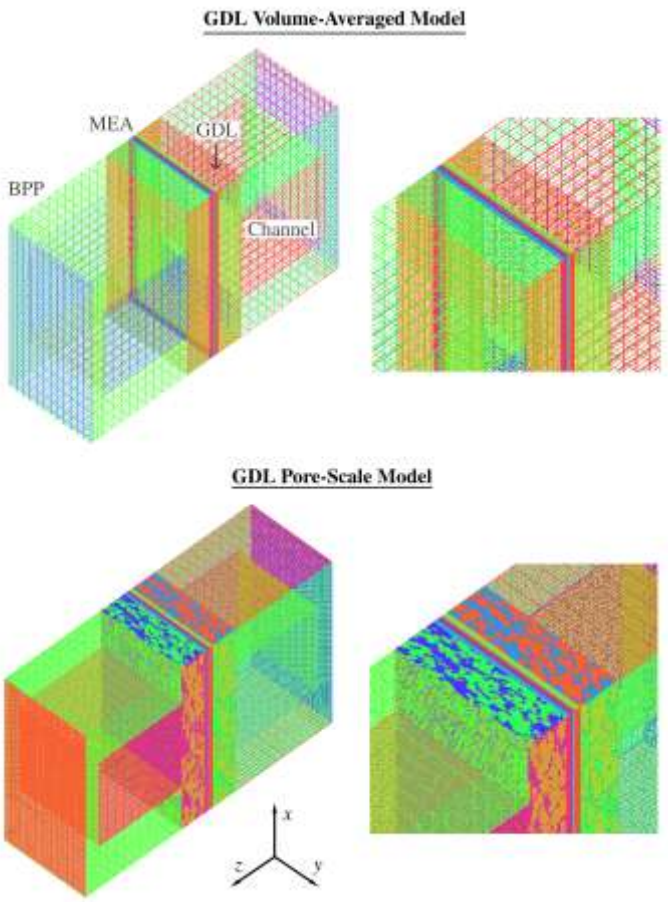

Figure 1: Meshes of the volume-averaged (VA) and pore-scale (PS) models. The modeled domain includes a 2×1 mm^2 elementary differential cell comprising the region between the mid-plane of two neighboring ribs. The location of the bipolar plate (BPP), membrane electrode assembly (MEA), gas diffusion layer (GDL) and channel is indicated.

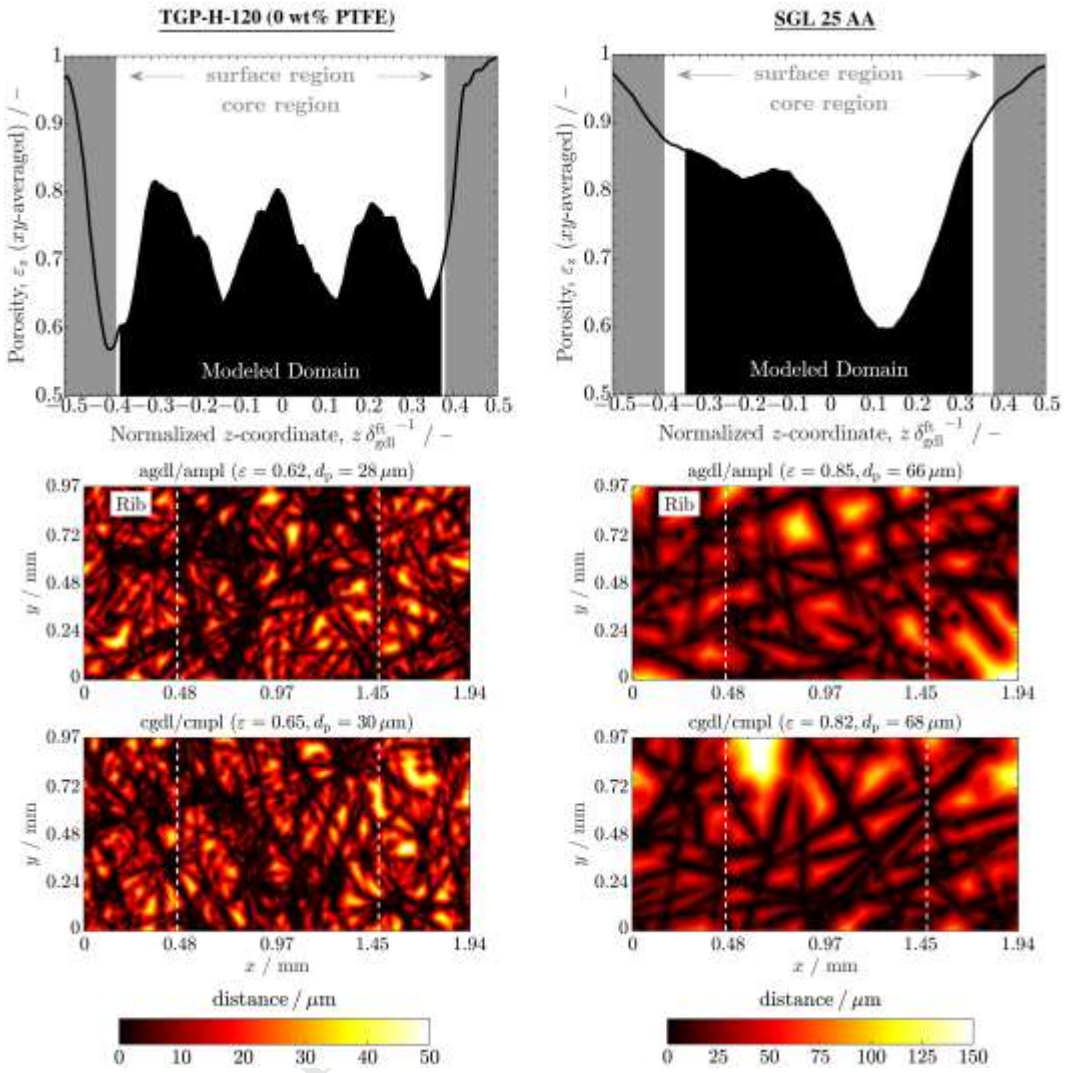

Figure 2: (upper plot) Through-plane (TP) porosity profiles, ε_z, corresponding to untreated TGP-H-120 ($\delta_{\mathrm{gdl}}/\delta_{\mathrm{gdl}}^{\mathrm{ft}} = 75\%$) and SGL 25 AA ($\delta_{\mathrm{gdl}}/\delta_{\mathrm{gdl}}^{\mathrm{ft}} = 67\%$), showing the modeled domain used in the simulations. The surface region is indicated by a grey background, while the core region is in white. (lower plot) Euclidean distance of the void space towards the solid phase at the anode and cathode GDL/MPL interfaces. The average interfacial porosity, ε, and pore diameter, d_p, are also indicated. The plotted distributions were averaged over the last 10 μm of the GDL facing the MPL (i.e., 10 slices of 1.3 μm thickness).

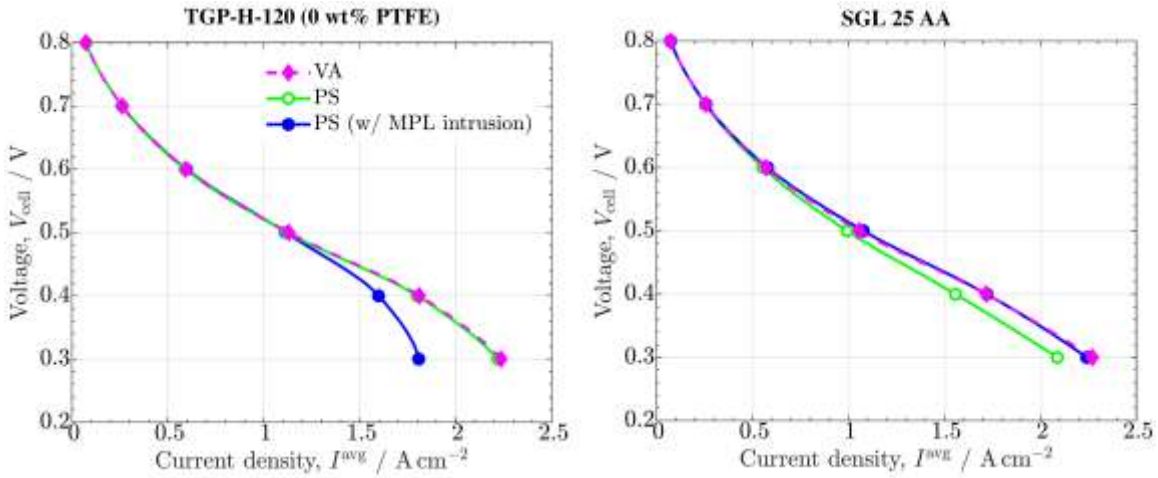

Figure 3: Polarization curves corresponding to untreated TGP-H-120 and SGL 25 AA, as predicted by the volume-averaged (VA) and pore-scale (PS) models. The results of the PS model considering a uniform intrusion between the MPL and the GDL are also included (see Section 4.3).

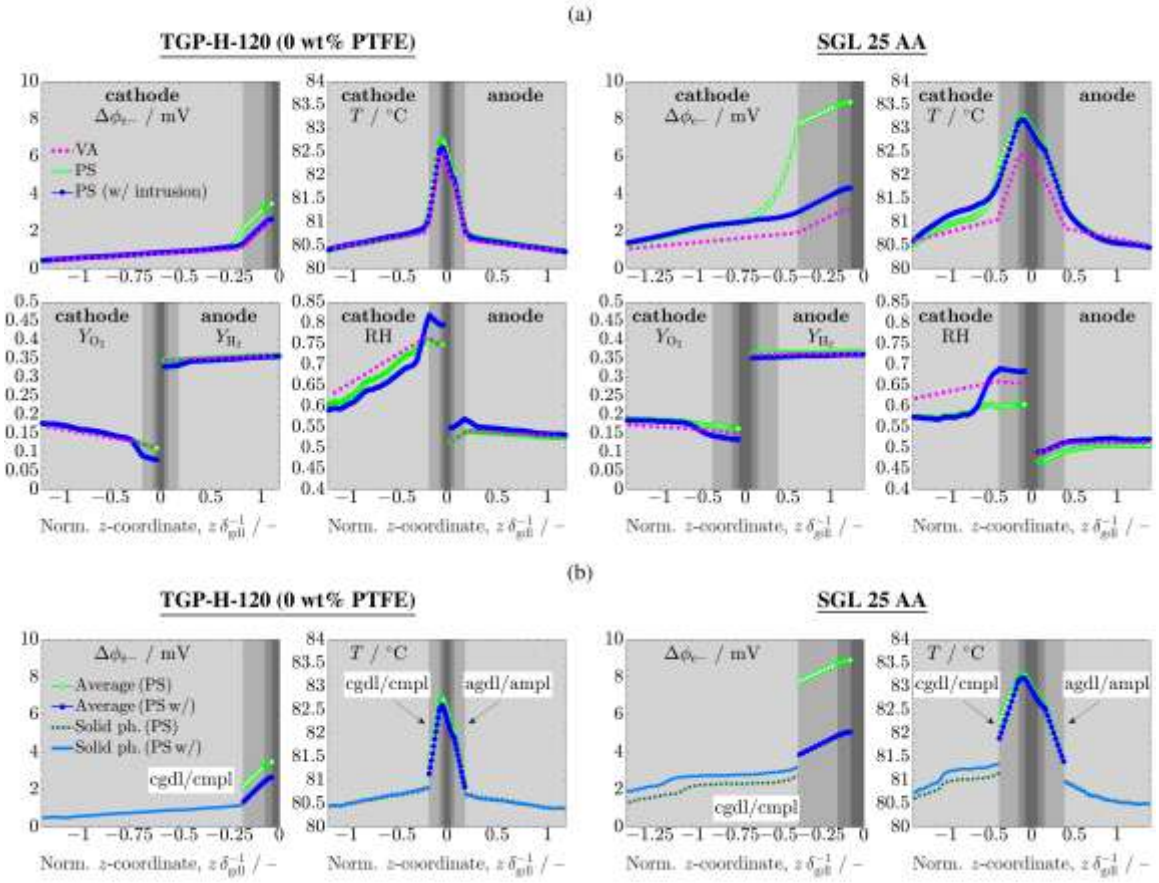

Figure 4: (a) Average through-plane (TP) profiles corresponding to untreated TGP-H-120 and SGL 25 AA, as predicted by the volume-averaged (VA) and pore-scale (PS) models at $V_{\mathrm{cell}} = 0.5$ V. The results of the PS model considering a uniform intrusion between the MPL and the GDL are also included (see Section 4.3). The plots show the cathode voltage drop, $\Delta\phi_{\mathrm{e}^-}(z)$, temperature, $T(z)$, oxygen/hydrogen mass fraction, $Y_{\mathrm{O}_2}(z)/Y_{\mathrm{H}_2}(z)$, and relative humidity, $\mathrm{RH}(z)$. The layers of the MEA (PEM, CLs, MPLs and GDLs) are indicated by dark to light gray patches, where $z = 0$ corresponds to the midplane of the membrane. (b) Cathode voltage drop, $\Delta\phi_{\mathrm{e}^-}(z)$, and temperature, $T(z)$, profiles of the VA components of the MEA (PEM, CLs and MPLs) and the solid phase of the GDL. The electrical and thermal contact resistance at the GDL/MPL interface leads to a sharp voltage and temperature drop between the MPL and the GDL solid phase, which is reduced when MPL intrusion into the GDL is taken into account.

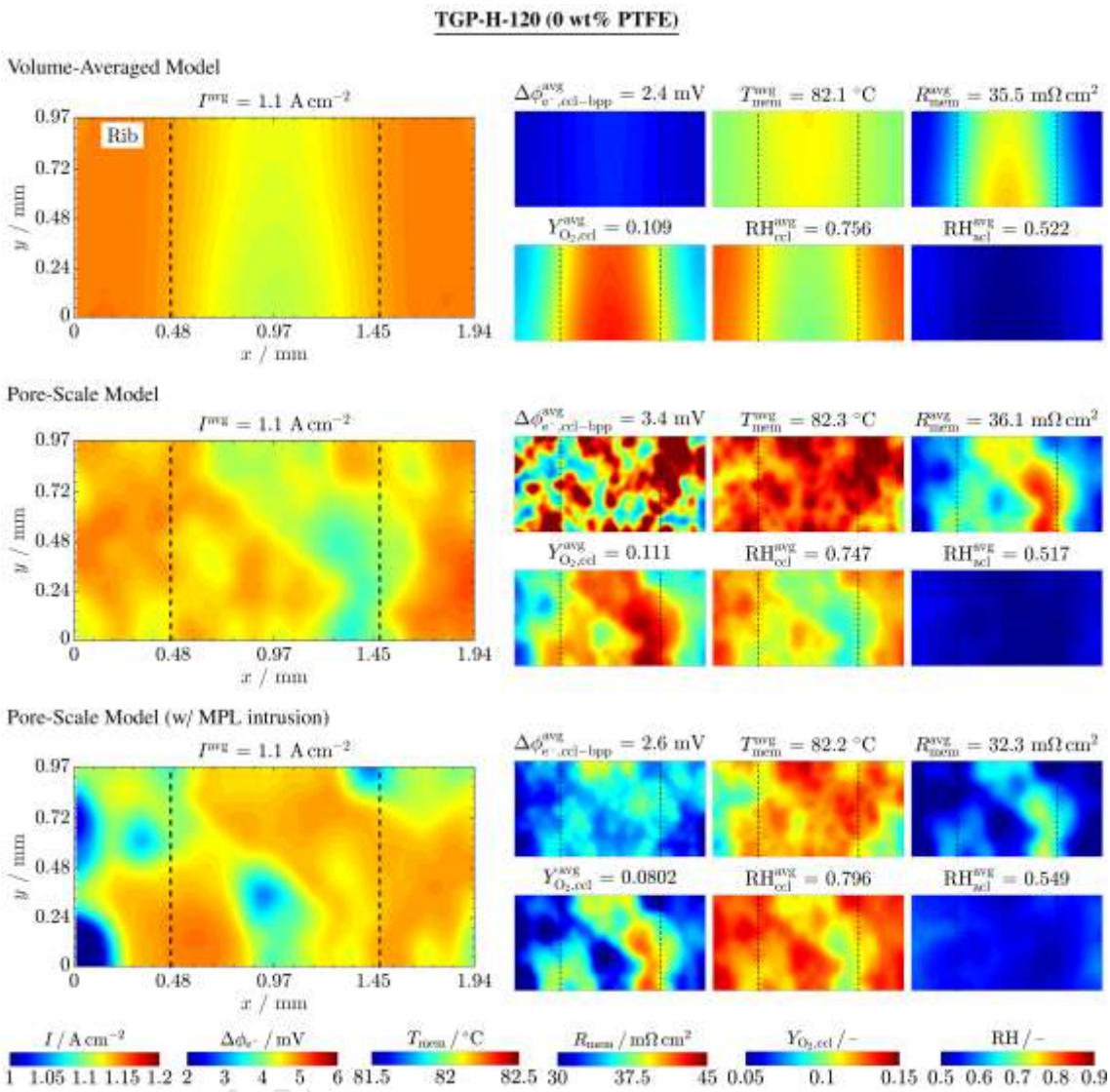

Figure 5: 2D in-plane distributions corresponding to untreated TGP-H-120, as predicted by the volume-averaged (VA) and pore-scale (PS) models at $V_{\text{cell}} = 0.5$ V. The results of the PS model considering a uniform intrusion between the MPL and the GDL are also included (see Section 4.3). The plots show the current density, $I(x,y)$, cathode voltage drop between the CL and the BPP, $\Delta\phi_{\text{e}^-,\text{ccl-bpp}}(x,y)$, temperature and ionic resistance of the membrane, $T_{\text{mem}}(x,y)$ and $R_{\text{mem}}(x,y)$, and oxygen mass fraction and RH in the CLs, $Y_{\text{O}_2,\text{ccl}}(x,y)$, $\text{RH}_{\text{ccl}}(x,y)$ and $\text{RH}_{\text{acl}}(x,y)$. The mean value of the distributions is indicated at the top of each subplot.

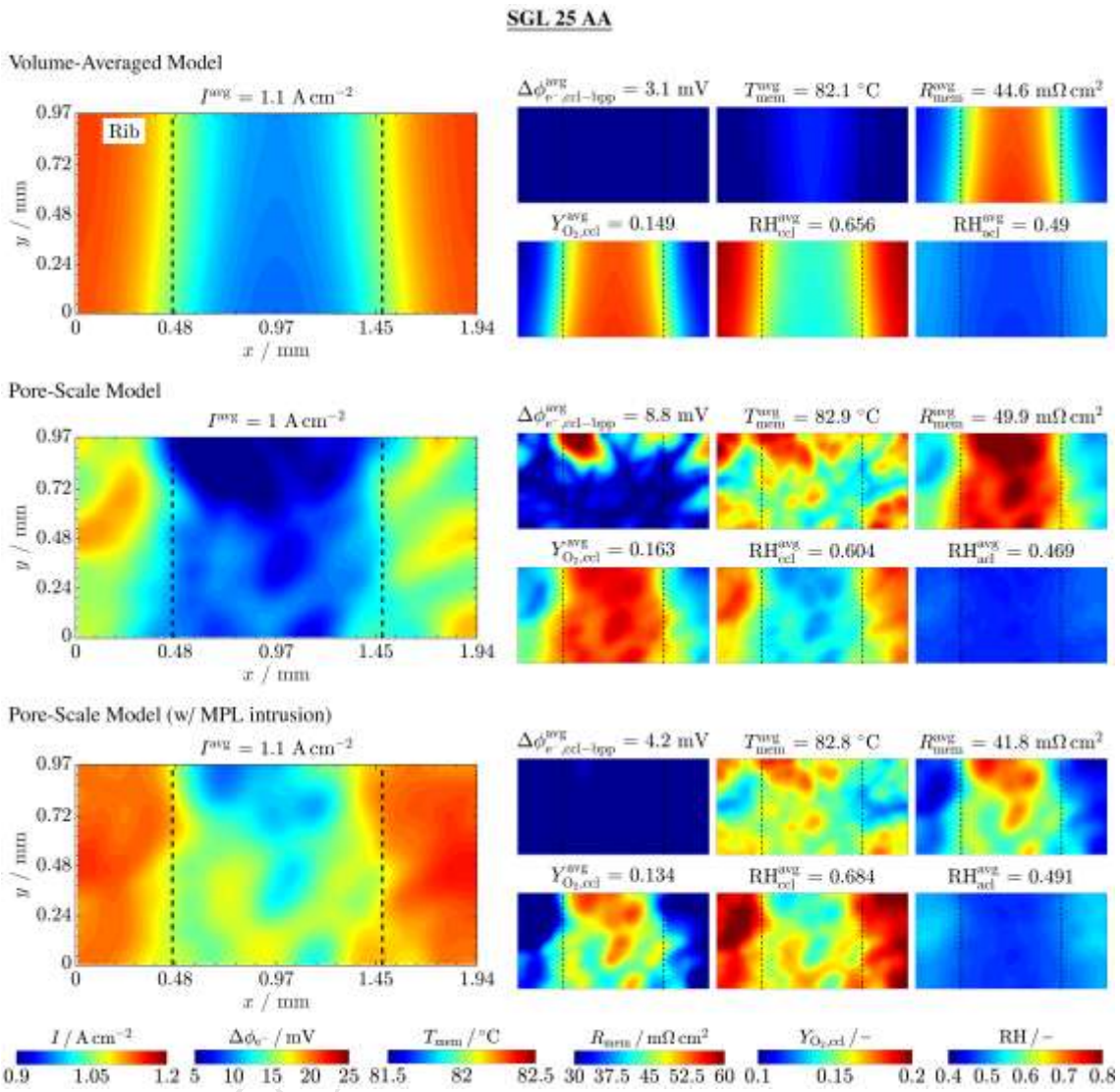

Figure 6: 2D in-plane distributions corresponding to SGL 25 AA, as predicted by the volume-averaged (VA) and pore-scale (PS) models at $V_{\text{cell}} = 0.5$ V. The results of the PS model considering a uniform intrusion between the MPL and the GDL are also included (see Section 4.3). See caption to Figure 5 for further details.

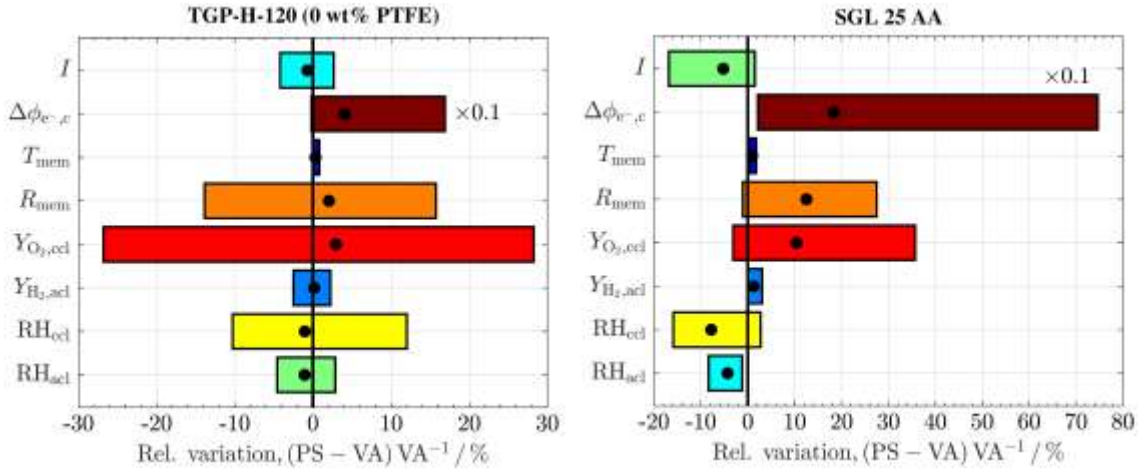

Figure 7: Relative variation of the spatial distributions between the pore-scale (PS) and volume-averaged (VA) models corresponding to untreated TGP-H-120 and SGL 25 AA for various variables of interest: current density, I, cathode voltage drop, $\Delta\phi_{e^-,c}$, temperature and ionic resistance of the membrane, T_{mem} and R_{mem}, oxygen and hydrogen mass fractions in the CLs, $Y_{O_2,ccl}$ and $Y_{H_2,acl}$, and relative humidity in the CLs, RH_{ccl} and RH_{acl}. The average value is indicated by a solid black dot. The variation of the cathode voltage drop was multiplied by 0.1 to facilitate visualization on the same scale. The bars are colored according to the extent of variation, while the spatial distributions can be seen in Figures 5 and 6.

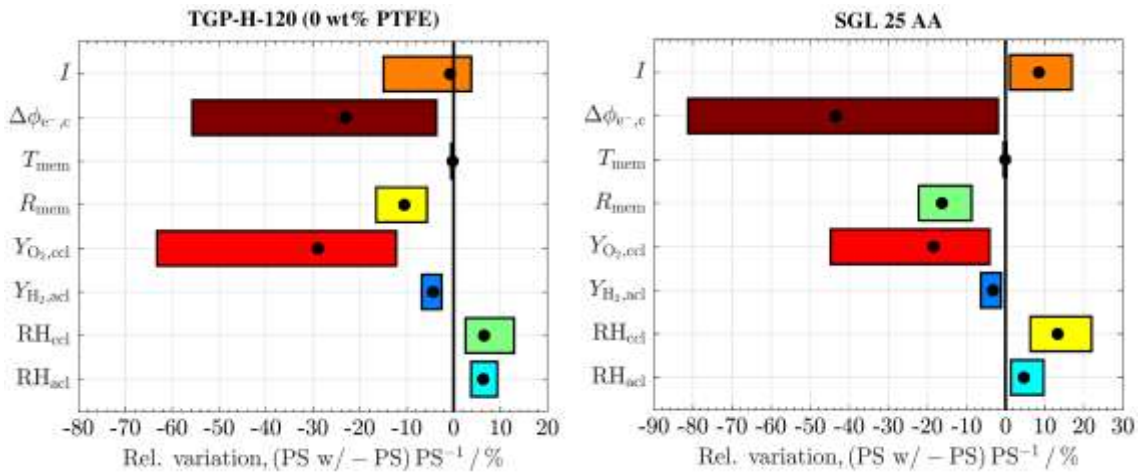

Figure 8: Relative variation of the spatial distributions between the pore-scale models with (PS w/) and without (PS) a uniform intrusion between the MPL and the GDL corresponding to untreated TGP-H-120 and SGL 25 AA for various variables of interest. The average value is indicated by a solid black dot. The bars are colored according to the extent of variation, while the spatial distributions can be seen in Figures 5 and 6. See caption to Figure 7 for further details.

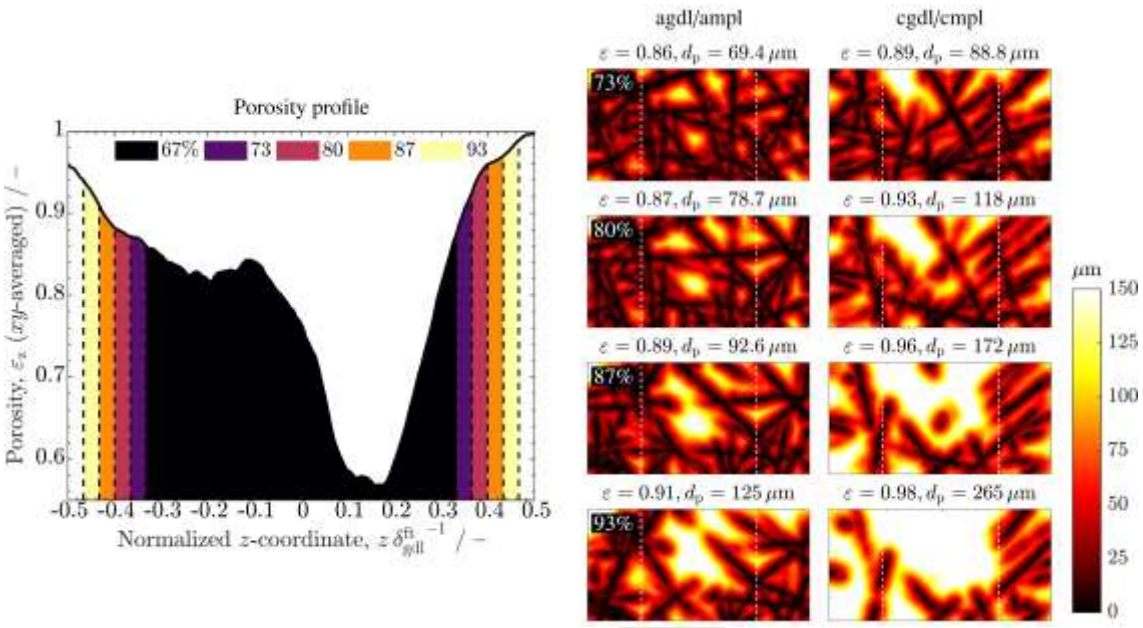

Figure 9: (left plot) Through-plane (TP) porosity profile, $\varepsilon_z(z)$, corresponding to SGL 25 AA, indicating the five GDL domains considered in the analysis of the surface region: $\delta_{\mathrm{gdl}} = 130\ \mu\mathrm{m}$ ($\delta_{\mathrm{gdl}}/\delta_{\mathrm{gdl}}^{\mathrm{ft}} = 67\%$), 143 μm (73%), 156 μm (80%), 169 μm (87%), 182 μm (93%). (right plot) Euclidean distance of the void space towards the solid phase at the anode and cathode GDL/MPL interfaces of the various domains. The range of the colormap is limited to 150 μm to facilitate visual comparison.

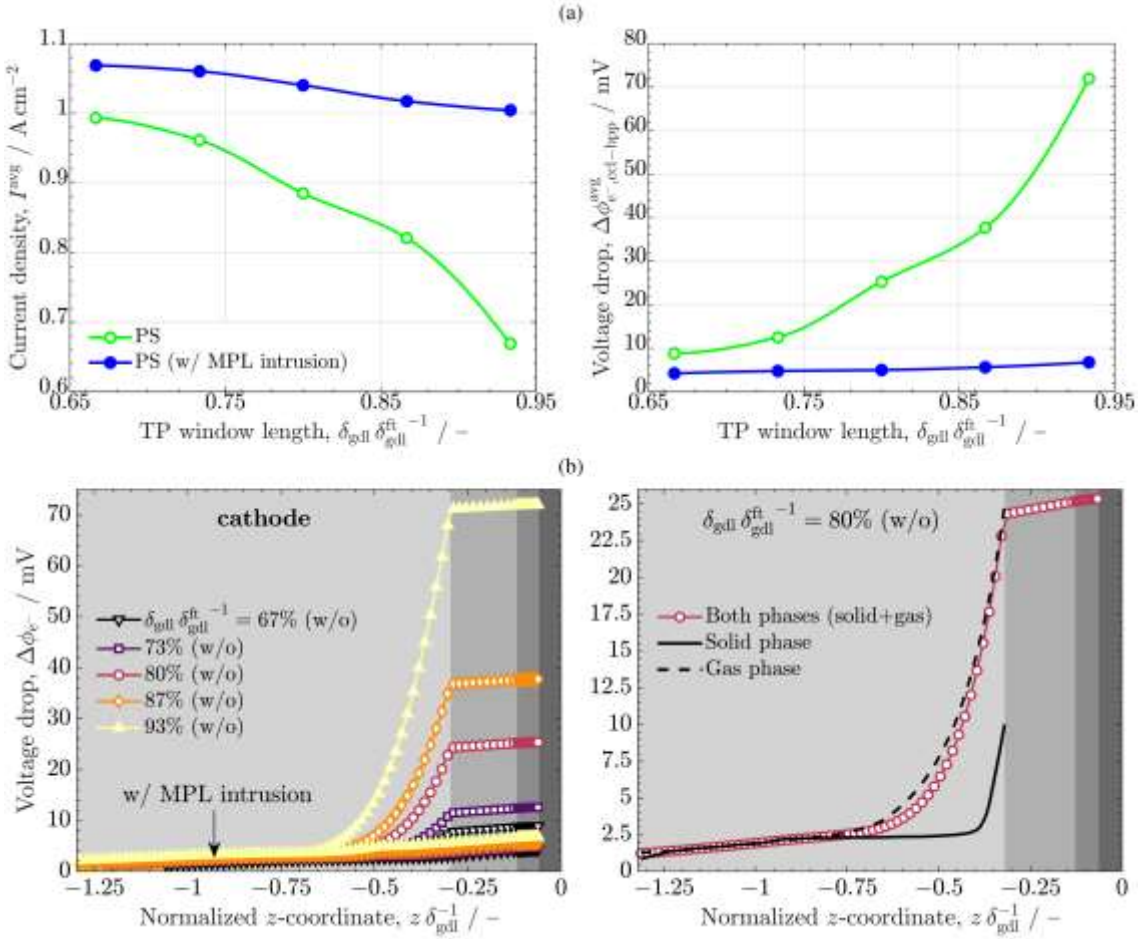

Figure 10: (a) Variation of the average current density, I^{avg}, and cathode voltage drop, $\Delta\phi_{\mathrm{e}^-,\mathrm{ccl-bpp}}^{\mathrm{avg}}$, with the GDL window length, $\delta_{\mathrm{gdl}}/\,\delta_{\mathrm{gdl}}^{\mathrm{ft}}$, as predicted by the pore-scale model without (PS) and with (PS w/) a uniform intrusion between the MPL and the GDL at $V_{\mathrm{cell}} = 0.5$ V. (b, left) Through-plane (TP) profiles of the cathode voltage drop, $\Delta\phi_{\mathrm{e}^-}(z)$, for different GDL window lengths, corresponding to the PS model. (b, right) $\Delta\phi_{\mathrm{e}^-}(z)$ for the case $\delta_{\mathrm{gdl}}/\delta_{\mathrm{gdl}}^{\mathrm{ft}} = 0.8$, as predicted by the PS model without GDL/MPL intrusion. The plot includes the average value of the solid and gas phases of the GDL, as well as the value of both phases separately. The layers of the cathode compartment (PEM, CL, MPL and GDL) are indicated by dark to light gray patches, where $z = 0$ corresponds to the midplane of the membrane. See caption to Figure 9 for further details.